Pure appl. geophys. 163 (2006) 975–994
0033–4553/06/060975–20
DOI 10.1007/s00024-006-0059-5

Pure and Applied Geophysics

Ultrasonic Velocities, Acoustic Emission Characteristics and Crack Damage of Basalt and Granite

SERGEI STANCHITS,[1] SERGIO VINCIGUERRA,[2] and GEORG DRESEN[1]

Abstract—Acoustic emissions (AE), compressional (*P*), shear (*S*) wave velocities, and volumetric strain of Etna basalt and Aue granite were measured simultaneously during triaxial compression tests. Deformation-induced AE activity and velocity changes were monitored using twelve *P*-wave sensors and eight orthogonally polarized *S*-wave piezoelectric sensors; volumetric strain was measured using two pairs of orthogonal strain gages glued directly to the rock surface. *P*-wave velocity in basalt is about 3 km/s at atmospheric pressure, but increases by $> 50\%$ when the hydrostatic pressure is increased to 120 MPa. In granite samples initial *P*-wave velocity is 5 km/s and increases with pressure by $< 20\%$. The pressure-induced changes of elastic wave speed indicate dominantly compliant low-aspect ratio pores in both materials, in addition Etna basalt also contains high-aspect ratio voids. In triaxial loading, stress-induced anisotropy of *P*-wave velocities was significantly higher for basalt than for granite, with vertical velocity components being faster than horizontal velocities. However, with increasing axial load, horizontal velocities show a small increase for basalt but a significant decrease for granite. Using first motion polarity we determined AE source types generated during triaxial loading of the samples. With increasing differential stress AE activity in granite and basalt increased with a significant contribution of tensile events. Close to failure the relative contribution of tensile events and horizontal wave velocities decreased significantly. A concomitant increase of double-couple events indicating shear, suggests shear cracks linking previously formed tensile cracks.

Key words: Acoustic emission, ultrasonic velocity, fracture, rock.

1. Introduction

The physical properties of rocks such as elastic constants and the speed of elastic waves are affected significantly by the volume, distribution and shape of the rock pore space (WALSH, 1965a; O'CONNELL and BUDIANSKY, 1974; PATERSON and WONG, 2005). In particular, it is well known that elastic wave velocities *P* and *S* may be reduced substantially in the presence of thin cracks (e.g., HADLEY, 1976). In a stressed rock volume, tensile cracks open preferentially normal to the

[1]Department 3.2, Geo Forschungs Zentrum Potsdam, Telegrafenberg D420, 14473, Potsdam, Germany. E-mail: stanch@gfz-potsdam.de
[2]Istituto Nazionale di Geofisica e Vulcanologia, Via di Vigna Murata 605, 00143, Rome, Italy. E-mail: vinciguerra@ingv.it

maximum compressive stress direction (TAPPONNIER and BRACE, 1976; RECHES and LOCKNER, 1994) resulting in an anisotropy of the elastic wave velocities. The speed of waves propagating in the direction normal to the planes of preferred crack orientation is more significantly decreased than the speed of waves travelling parallel to the crack planes (NUR, 1971; BONNER, 1974; LOCKNER *et al.*, 1977; SCHUBNEL *et al.*, 2003). Assuming transverse isotropy observed elastic wave speeds may be used to estimate the respective anisotropic elastic constants and crack damage (MAVKO *et al.*, 1998; SOGA *et al.*, 1978; AYLING *et al.*, 1995; SCHUBNEL *et al.*, 2003). HADLEY (1976) observed a significant decrease of *P*-wave and *S*-wave speeds and comparable changes in velocity ratios with increasing dilatancy in both Westerly granite and San Marcos gabbro. Upon unloading, plots of velocities versus volumetric strain showed a hysteresis with lower velocities during unloading. In general, the experimental studies show that wave velocities increase with increasing confining pressure and decrease with increasing deviatoric stresses; both observations have been related to the pressure-induced closure and stress-induced opening of narrow cracks (e.g., GUEGUEN and PALCIAUSKAS, 1994; PATERSON and WONG, 2005).

Mount Etna with its diameter of 40 km and its height of $\sim$ 3300 m is the largest volcano in Europe, characterized by mostly effusive eruptions constituting a major natural hazard for human settlements in the Etna region. Overpressured magma stored in shallow reservoirs and time-dependent failure of the country rock, induce bursts of seismic activity and episodes of ground deformations that occur from years to months before a new major eruption. Recent pre-eruptive stages have been closely monitored by using both ground deformation and seismic arrays (CASTELLANO *et al.*, 1993; FERRUCCI *et al.*, 1993; BRIOLE *et al.*, 1990; BONACCORSO *et al.*, 1990). The observations have been related to increasing damage and a changing stress field within the volcanic edifice largely consisting of basalt. However, the mechanical behavior of Etna basalt and the effect of deviatoric stresses on crack damage and elastic wave velocities are not well understood. Previous laboratory measurements of *P*-wave and *S*-wave velocities were solely performed at hydrostatic pressures up to 80 MPa and indicate that Etna basalt contains substantial crack damage (VINCIGUERRA *et al.*, 2005). Crack densities inverted from velocity measurements at increasing pressure (BENSON *et al.*, 2006; SCHUBNEL *et al.*, this issue), manifest a progressive closure of the cracks.

Here we combine laboratory measurements of elastic wave velocities (*P* and *S*) at varying confining pressures up to 120 MPa and under deviatoric stresses increased to sample failure with an analysis of acoustic emissions (AE) recorded during the experiments. We determined the location and AE source types in experiments performed on Etna basalt and Aue granite at identical loading conditions. Aue granite was used as a reference material containing low initial crack damage and low porosity. Anisotropic elastic constants, crack damage and crack types are estimated from the data.

2. Experimental Techniques

2.1 Sample Material and Testing Procedure

Experiments were performed on cores drilled from typical Etna basalt and on granite samples from Aue, Germany. Etna basalt (EB) is a porphyritic alkali basalt from Mount Etna, Italy, containing mm-sized phenocrysts of pyroxene, olivine and feldspar in a fine-grained groundmass. Initial density is 2.86 ± 0.01 g/cm^3 and porosity is $2.1 \pm 0.1\%$. The granite has an initial density of 2.62 g/cm^3 and an initial porosity of 1.3%. Mineral composition of granite contains 30% quartz, 40% plagioclase, 20% potassium feldspar and 10% mica (ZANG *et al.*, 2000). The grain size ranges from 0.9 mm to 1.8 mm with an average value of 1.3 mm (Fig. 1). Microstructure analysis of undeformed Aue granite yielded crack densities in the range of 0.3–0.6 mm^{-1} (JANSSEN *et al.*, 2001). No data exist for the Etna basalt, however, the block from which samples were cored contains abundant mm- to cm-scale cracks that possibly result from rapid cooling (VINCIGUERRA *et al.*, 2005).

Cylindrical samples of Etna basalt and Aue granite with a diameter of 50 mm and 100 mm in length were subjected to two types of loading: All samples were first subjected to hydrostatic pressure ($\sigma_1 = \sigma_2 = \sigma_3$) increasing from 5 MPa up to 120 MPa and subsequently decreasing to 60 MPa. Pressure changes were performed at a rate of 1.5 MPa per minute. Subsequently, an axial stress was applied to the specimens. The samples were subjected to three stress cycles at decreasing confining pressures of 60, 40 and 20 MPa, respectively, in a servo-controlled 4600 kN MTS loading frame (Fig. 2a). At the lower confining pressures, samples were loaded until catastrophic failure occurred.

Volumetric strain was estimated using two pairs of strain gages glued directly onto the sample surface. The strain gages were oriented parallel to the sample axis (ε_1) and in a circumferential direction (ε_3) (Fig. 3). Volumetric strain Δ was calculated using: $\Delta = \varepsilon_1 + 2\varepsilon_3$. Axial strain ε_1 was calculated using the average values of the two vertically oriented strain gages. Compaction is indicated by $\Delta > 0$ and dilatancy by $\Delta < 0$.

Axial loading rate was servo-controlled using the AE rate recorded by a piezoceramic sensor attached to the sample. For AE rates below a defined trigger level, the displacement rate was set to 0.02 mm/min. When the AE rate exceeds the trigger level the displacement rate is decreased significantly to about 10^{-10} mm/min. The threshold level of the rate control sensor allowed variation of the speed of fault propagation by three orders of magnitude, i.e., from mm/s in fixed displacement rate tests to μm/s in AE rate-controlled tests.

2.2. Velocity and Acoustic Emission Monitoring

AE activity and velocity changes were monitored by twelve *P*-wave and eight *S*-wave piezoelectric sensors either embedded in the pistons or glued to the sample

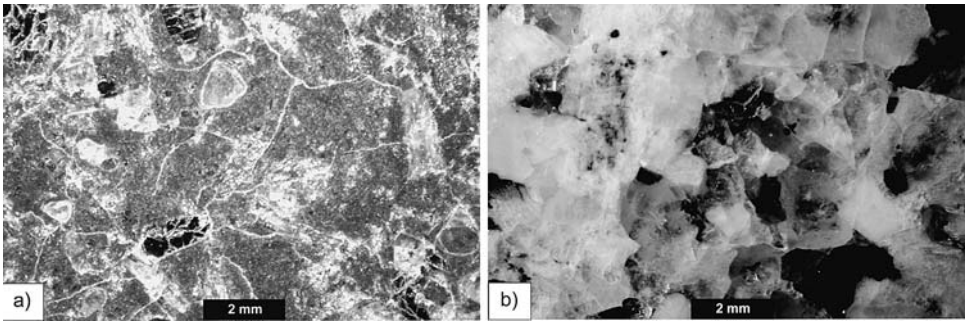

Figure 1
Optical micrograph (crossed polars) of Etna basalt (a) and Aue granite (b). Note array of mm-scale cracks in basalt.

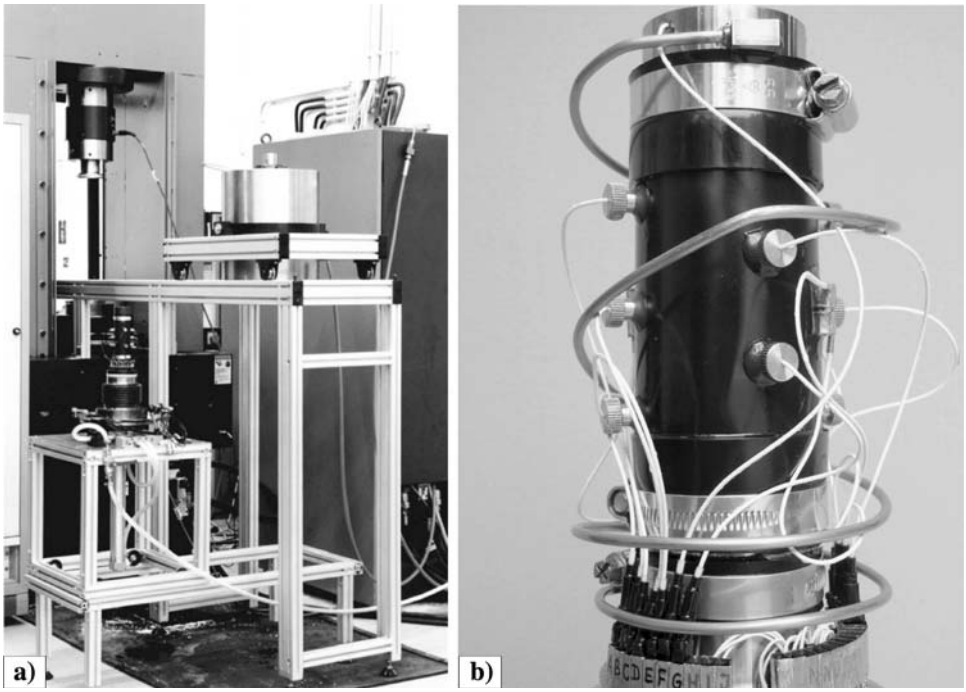

Figure 2
Experimental setup. (a) MTS loading frame with 200 MPa pressure vessel. (b) Cylindrical specimen encapsulated in rubber jacket with *P* and *S* sensors glued directly to the sample surface. For velocity measurements parallel to sample axis, two *P* sensors were embedded in upper and lower endcaps.

surface and sealed in a Neoprene jacket using two-component epoxy (Fig. 2b). *P*-wave velocities were measured parallel (P_V) and normal (P_H) to the loading direction. To analyze stress-induced shear-wave splitting, we installed four S-wave piezoelectric sensors polarized in the vertical direction (S_{HV}) and horizontal direction

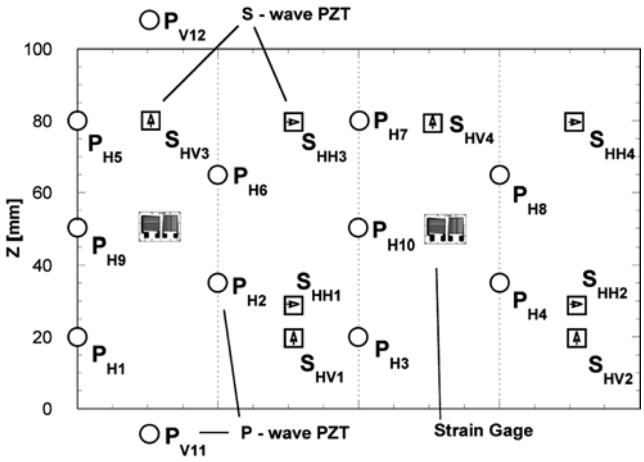

Figure 3
Projected sample surface showing position of 20 ultrasonic sensors and 4 strain gages installation (Z is sample axis). P_H and P_V are piezoelectric sensors measuring *P*-wave velocity in horizontal and vertical directions. S_{HH} are shear sensors polarized in horizontal direction, S_{HV} are shear sensors polarized in vertical direction.

(S_{HH}), respectively. The first index on *P* and *S* indicates wave propagation direction and the second index on *S* indicates the plane of polarization. The piezoelectric sensors were manufactured at the GFZ and tested at confining pressures up to 200 MPa. *P*- and *S*-wave sensors were produced from PZT piezoceramic discs with 5 mm diameter and 1 mm thickness and square shape piezoceramic plates $5 \times 5 \times 1$ mm, respectively. The thickness and diameter-related resonant frequencies of the *P*-wave sensors are about 2 MHz and 500 KHz, respectively.

Transducer signals are amplified by 40 dB using Physical Acoustic Corporation (PAC) preamplifiers equipped with 100 kHz high-pass filters. Full-waveform AE data and the ultrasonic signals for *P*-wave velocity measurements are stored in a 12 channel transient recording system (PRÖKEL, Germany) with an amplitude resolution of 16 bit at 10 MHz sampling rate. *S*-wave sensors were connected to a separate transient recorder (KRENZ, Germany, 10 bit amplitude resolution, 10 MHz sampling rate) (Fig. 4). For periodic elastic wave speed measurements we used six *P*-sensors and four *S*-sensors as senders applying 100 V pulses every 30–40 seconds during loading. Ultrasonic transmissions and AE waveforms were discriminated automatically after the experiments.

The AE recording system is equipped with a 6 Gb memory buffer for temporary storage during the experiments that allows recording of digitized waveforms of 256 thousand AE signals with a length of about 100 μs. Continuous AE recording with zero dead time between consecutive signals is possible. For AE hypocenter location, *P*-wave onset time is picked automatically using different criteria including Akaike's

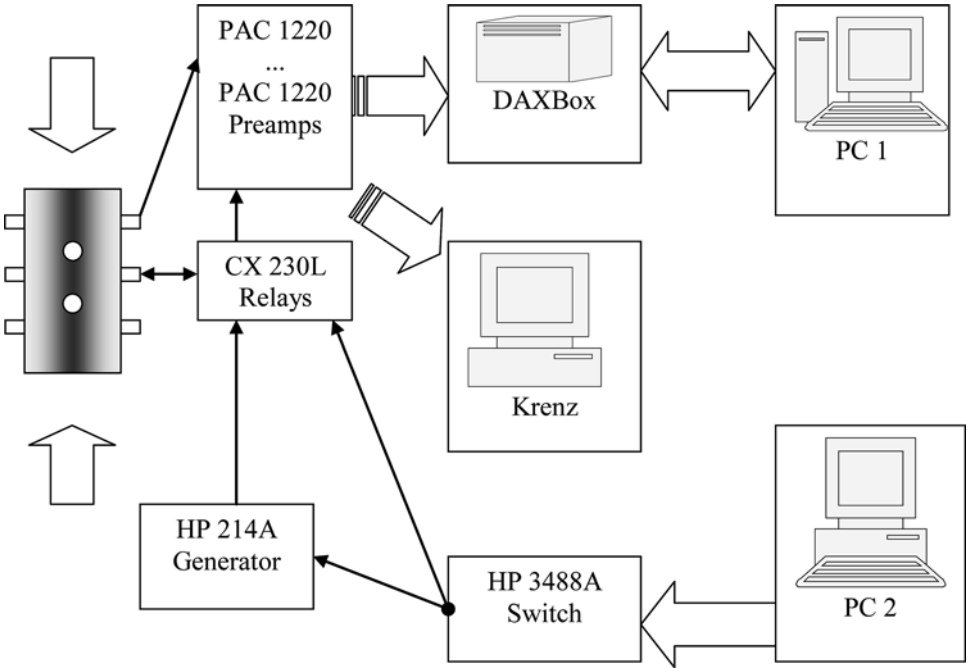

Figure 4
Block diagram of experimental setup to monitor acoustic emission activity and ultrasonic transmission.

information criterion (LEONARD and KINNETT 1999). An automatic minimization procedure of travel-time residuals was used to exclude noisy channels and decide for the preferred onset time criterion. Hypocenter locations were estimated using a downhill simplex algorithm (NELDER and MEAD, 1965) considering time-dependent changes of the anisotropic velocity field. We estimate the AE location accuracy to be 2.5 mm. First motion amplitudes were picked automatically and first motion polarities were used to discriminate AE source types in tensile, shear and collapse events (ZANG *et al.*, 1998).

3. Experimental Results

3.1. Hydrostatic Loading

Compaction of the basalt samples at 120 MPa pressure is $\approx 0.8\%$ and about twice that of the granite samples ($\Delta \approx 0.4\%$). With increasing pressure the elastic wave speeds P and S increased (Figs. 5a-f). The maximum difference in wave speeds in different directions was $<2\%$ and close to experimental error. Therefore we

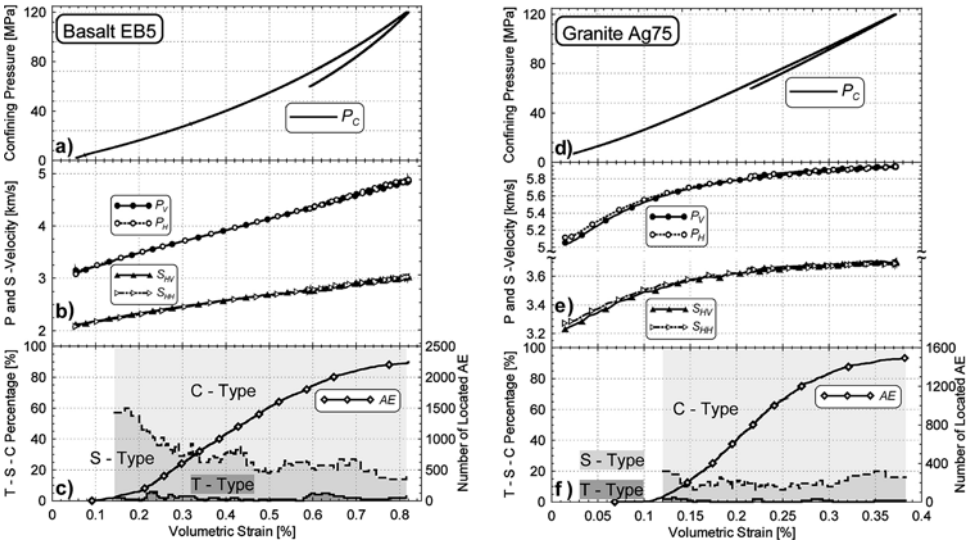

Figure 5
Plot of confining pressure, elastic velocities, cumulative AE number and AE types versus volumetric strain during hydrostatic loading of Etna basalt EB5 and Aue granite Ag75. Volumetric strain was calculated as $\Delta = \varepsilon_1 + 2\varepsilon_3$, where ε_1 and ε_3 are axial and horizontal components of the strain measured during the experiment. Separation of tensile, shear and collapse types of AEs was performed using AE first motion polarity analysis. Estimated error of velocity measurements corresponds approximately to the size of symbols on plots b) and e).

consider the velocity field to be isotropic. Horizontal *P*-wave velocities (P_H) and the *S*-wave components (S_{HH} and S_{HV}) were averaged from five and two horizontal traces, respectively. In granite, *P*- and *S*-wave velocities approach maximum values of about 6 km/s and 3.7 km/s with increasing pressure and compaction of the sample (Fig. 5). However, in basalt velocities show a continuous increase with pressure up to 120 MPa. With increasingly confining pressure, *P*-wave velocities in basalt increased by about 50% (from 3.1 to 4.8 km/s), however in granite *P*-wave speeds increased only by about 18% (from 5.05 to 5.94 km/s).

Significant AE activity was observed during compaction of the basalt and granite samples starting at relatively small volumetric strains of 0.1–0.2%. AE hypocenter distribution is almost random, suggesting that compaction is relatively homogeneous. The relative source type distribution reveals a dominance of pore collapse (C-type) sources and about 20% double-couple (S-type) shear events. The contribution of shear type events during compaction is higher in basalt than in granite, in particular at low volumetric strain. AE activity, AE source types and the hysteresis in the plot of confining pressure versus volumetric strain all indicate that crack closure during hydrostatic loading is not purely elastic but produces some irreversible deformation (Fig. 5).

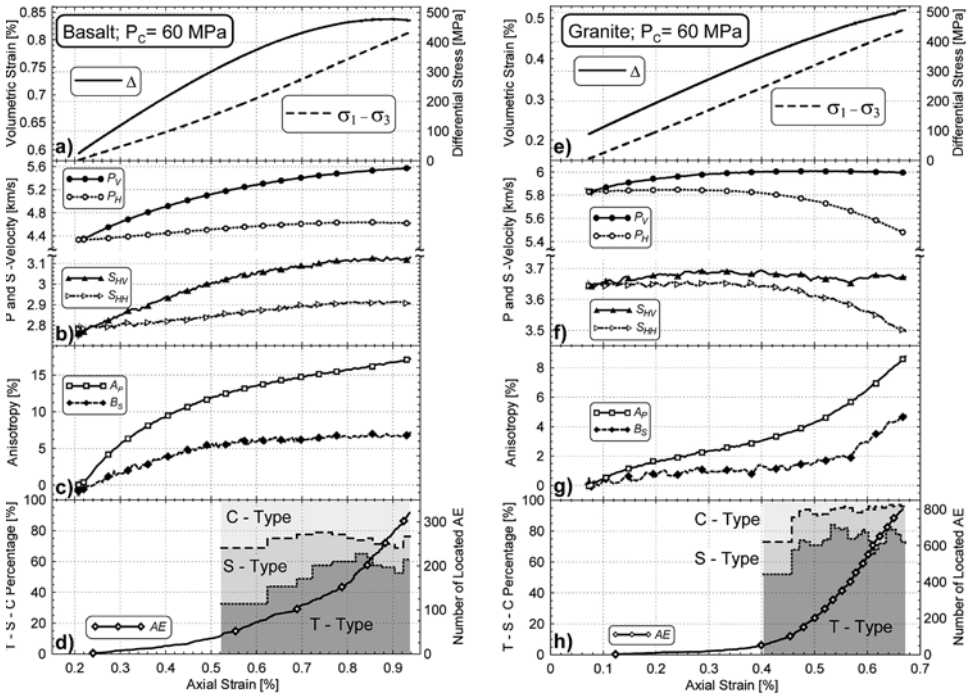

Figure 6
Plot of volumetric strain, elastic velocities, *P*-wave anisotropy, *S*-wave birefringence, cumulative AE number and AE source types versus axial strain during loading of Etna basalt EB5 and granite Ag75 at 60 MPa confining pressure (see text for details).

3.2. Axial Compression Testing

The basalt and granite specimens were subjected to increasing stresses in three consecutive cycles at decreasing confining pressures of 60 MPa, 40 MPa and 20 MPa. The first two cycles were interrupted at differential stresses of about 500 MPa and axial strains between 0.7% – 0.8%. During the third cycle the specimens were loaded to failure. With increasing axial stress and strain, basalt and granite samples show initial overall compaction, but at smaller confining pressures and at axial strains $\varepsilon_1 > 0.7\%$ dilatant cracking becomes increasingly important $\left(\frac{d\Delta}{d\varepsilon_1} < 0\right)$ (Fig. 8a). Maximum compaction of the basalt samples reached during each load cycle decreases with decreasing confining pressure but always remains higher than for granite.

At all confining pressures *P*- and *S*-wave velocities in basalt and granite manifest significant anisotropy (Figs 6–8). In general, P_V -wave speeds are higher than P_H – velocities, and *S*-waves show acoustic birefringence (NUR, 1971; BONNER, 1974; HADLEY, 1975; LOCKNER *et al.*, 1977) with S_{HV} always being faster than S_{HH}. We define anisotropy and birefringence as $A_P = \frac{(P_V - P_H)}{P_V}$ and $B_S = \frac{(S_{HV} - S_{HH})}{S_{HV}}$, respectively. *P*-wave anisotropy and *S*-wave birefringence increase with increasing axial stress and

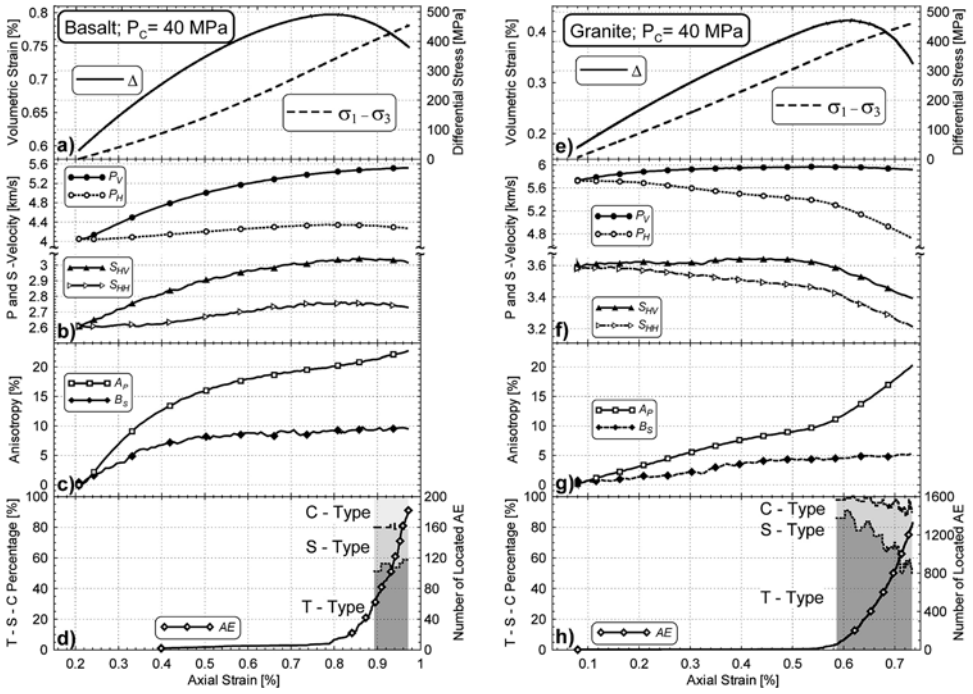

Figure 7
Plot of volumetric strain, elastic velocities, *P*-wave anisotropy, *S*-wave birefringence, cumulative AE number and AE types versus axial strain during loading of Etna basalt EB5 and granite Ag75 at 40 MPa confining pressure (see text for details).

axial strain and as samples approach failure. These observations suggest that stress-induced cracks are mainly vertically oriented with crack plane normal directions defining a zone perpendicular to the axial stress direction. However, changes in wave speeds are significantly more pronounced in basalt than in granite. With increasing stress and axial strain, *P*-wave anisotropy and *S*-wave birefringence exhibit different behavior in basalt and granite (Figs. 6–8). For example, at all confining pressures and at low stresses, anisotropy and birefringence increase more rapidly in basalt than in granite. However, at elevated stresses and larger axial strain, anisotropy increases more strongly in granite than in basalt.

Acoustic emission activity during loading cycles shows a pronounced Kaiser effect (HOLCOMB, 1993) (Figs. 6–8). For granite, the onset of AE activity is associated with a change in the slope of P_H and S_{HH} velocities versus axial strain (Figs. 6h–8h). The effect is less pronounced for basalt (Figs. 6d–8d). Acoustic emission source types are distinctly different from those found at hydrostatic compaction (Fig. 5). With increasing axial stress and decreasing confining pressure, *T*-type events are dominant in both basalt and granite specimens. Close to failure, however, double-couple *S*-type events become increasingly important. The contribution of *C*-type events related to

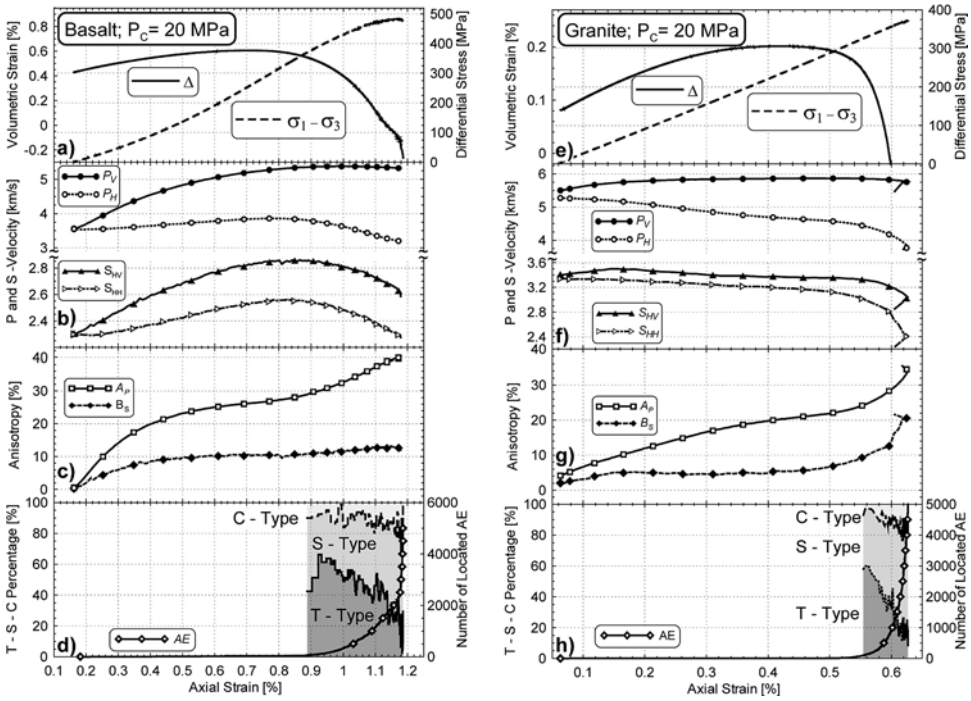

Figure 8
Plot of volumetric strain, elastic velocities, *P*-wave anisotropy, *S*-wave birefringence, cumulative AE number and AE types versus axial strain during loading of Etna basalt EB5 and granite Ag75 at 20 MPa confining pressure. The sample was loaded up to failure (see text for details).

collapsing pore space in basalt during loading at 40 and 60 MPa is 10%–20%, and < 5% in granite.

4. Discussion

4.1. Hydrostatic Compaction of Basalt and Granite

The effective dynamic and static elastic Young's modulus E_{eff}, bulk modulus K_{eff} and the Poisson ratio v_{eff} of basalt and granite increase with increasing pressure (Fig. 9) and show a hysteresis when pressure is released. The dynamic moduli are estimated using the equations:

$$v_{eff} = \left[\left(\frac{P}{S}\right)^2 - 2\right] \Big/ \left[\left(\frac{P}{S}\right)^2 - 1\right], \tag{1}$$

$$K_{eff} = \rho\left(P^2 - \frac{4}{3}S^2\right), \tag{2}$$

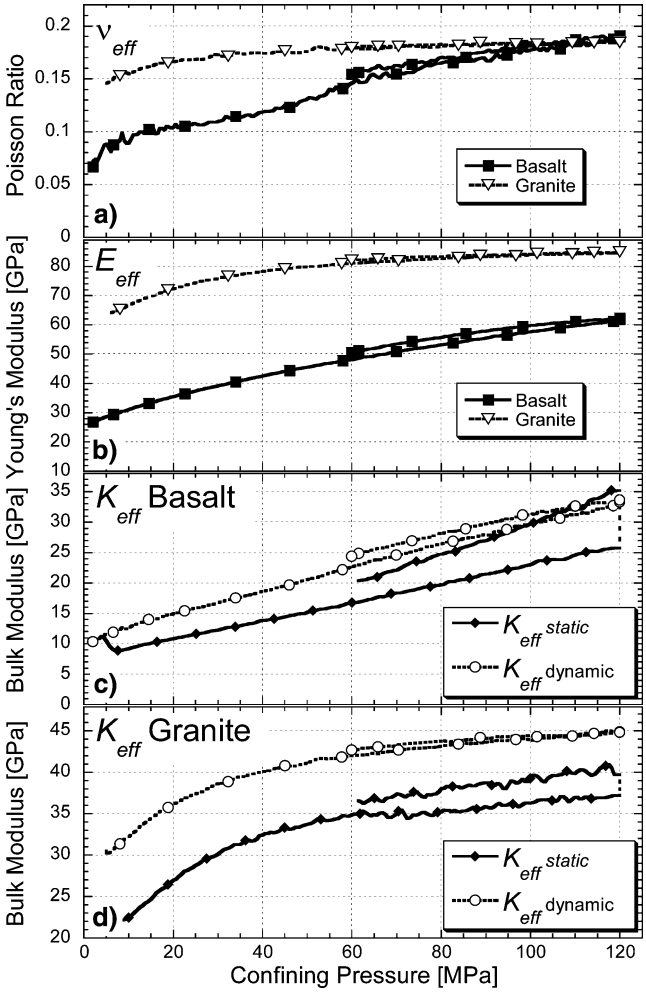

Figure 9
Effective Poisson ratio, Young's modulus and bulk modulus, calculated from elastic wave velocities (dynamic parameters) and mechanical measurements (static parameters) during hydrostatic loading of Basalt Eb5 and Granite Ag75. Samples were first pressurized to 120 MPa and then pressure was reduced to 60 MPa.

$$E_{eff} = 3K_{eff}\left(1 - 2v_{eff}\right), \tag{3}$$

where ρ is density and P, S are average P-wave and S-wave speeds. The static bulk modulus was also estimated from the change of volumetric strain $d\Delta$ with increasing pressure dP_c:

$$K_{eff} = \frac{dP_C}{d\Delta}. \tag{4}$$

The elastic moduli are somewhat higher when estimated during unloading than during loading. This corresponds to a small hysteresis of the wave speed versus volumetric strain relation between loading and unloading. In contrast to loading cycles at differential stress (see below, HADLEY, 1975) velocities remain slightly higher during unloading. Compaction of the basalt and granite samples with increasing hydrostatic pressure is associated with high AE activity and dominantly *C*- and *S*-type AE sources. This suggests that compaction of the samples involves irreversible pore collapse and frictional sliding along pre-existing defects.

For the same sample at similar pressures, static bulk moduli are smaller and show a larger hysteresis with increasing and decreasing confining pressure than the dynamic moduli. Static bulk moduli of dry rocks are often found to be lower than dynamic values although the effect is not well understood (SIMMONS and BRACE, 1965; KING, 1969; CHENG and JOHNSTON, 1981). Often the observed difference between static and dynamic moduli decreases with increasing pressure and is commonly attributed to the presence of cracks. Possibly, larger strain amplitudes for static measurements may produce inelastic effects that are not observed during dynamic measurements (DRESEN and GUEGUEN, 2004). For example, irreversible mechanical compaction and interlocking of crack faces may explain the observed hysteresis of velocities and elastic moduli between loading and unloading cycles (WALSH, 1965b). Deformation of crack asperities and the effect of frictional contacts may differ significantly for strains that are several orders of magnitude larger for static compared to dynamic measurements.

At elevated confining pressure > 80 MPa the bulk modulus for granite remains almost unchanged, but for basalt K_{eff} continues to increase almost linearly with pressure, suggesting that low aspect ratio cracks contribute significantly to the basalt total porosity. The effective compressibility of a rock is mostly affected by compliant cracks and less by stiff spherical pores (WALSH, 1965a). To estimate the contribution of crack porosity to the bulk porosity estimated using Archimedes method we use the approach of WALSH (1965a). The initial crack porosity is estimated graphically (Fig. 10). In granite, the crack porosity (0.07%) is approximately 20 times smaller than the total unconnected porosity (1.3%). In basalt the compliant crack porosity (0.46%) is approximately only 5 times smaller than the total porosity (2.1%). The contribution of crack porosity to the total porosity is significantly larger for basalt than for granite, which is in agreement with preliminary microstructure observations. Granite contains predominantly intergranular cracks. Etna basalt contains abundant long and thin cracks that formed during rapid cooling and spheroidal pores possibly produced from lava degassing (Fig. 1). However, the effect of these spheroidal pores on the bulk modulus is probably subordinate; for example, a total porosity of 2.1% contained in spherical pores reduces the bulk modulus by $< 5\%$ (WALSH, 1965a).

Background crack densities estimated from the microstructure at atmospheric pressure only exist for undeformed Aue granite (JANSSEN *et al.*, 2001), ranging between 0.3–0.6 mm^{-1}. However, to assess decreasing crack density with increasing

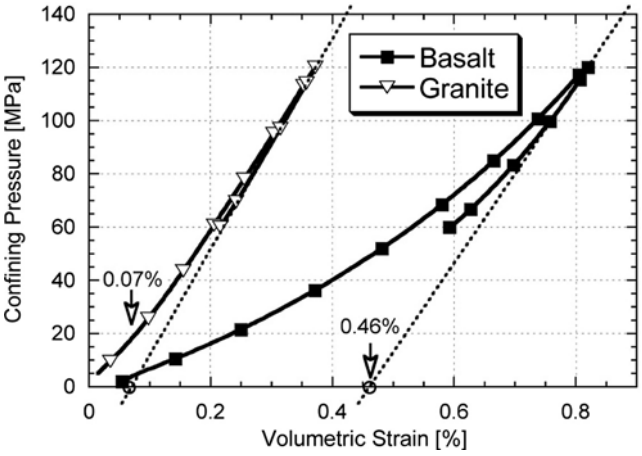

Figure 10
Hydrostats of Basalt Eb5 and Granite Ag75. Crack porosity was estimated graphically (WALSH, 1965a); for granite the crack porosity is 0.07% compared to 1.3% total porosity, for basalt the crack porosity is 0.46% compared to 2.1% total porosity.

confining pressure we compare the results from Walsh's mechanical crack closure model with crack densities predicted from seismic velocities using self-consistent theory. The studies of WALSH (1965a,b) and O'CONNELL and BUDIANSKY (1974) analyze the effect of cracks on the elastic properties of rocks. A central assumption in both models is that crack density is low, crack interaction may largely be neglected and crack distribution in the rock is isotropic. The density of low aspect ratio cracks is defined as:

$$\Gamma = N\langle c\rangle^3. \tag{5}$$

N is the number of cracks per unit volume and $\langle c\rangle$ is the mean crack radius. Crack density may be estimated using mechanical closure data or wave speeds from the equation (WALSH, 1965a):

$$\Gamma = \frac{9}{16}\frac{(1-2\nu_0)}{(1-\nu_0^2)}\left(\frac{K_0}{K_{eff}}-1\right), \tag{6}$$

where K_0 and ν_0 are the bulk modulus and Poisson ratio of the crack-free rock, respectively. In the self-consistent model of O'CONNELL and BUDIANSKY (1974) it is assumed that the cracks are contained in a cracked matrix with as-yet-unknown effective elastic properties. Crack density may then be estimated from the effective bulk modulus and Poisson ratio:

$$\Gamma = \frac{9}{16}\frac{(1-2\nu_{eff})}{(1-\nu_{eff}^2)}\left(1-\frac{K_{eff}}{K_0}\right). \tag{7}$$

For comparison we also apply the model of SOGA *et al.* (1978) to invert crack densities from the velocity data. This model is largely based on the numerical calculation of effective elastic constants of a cracked solid by ANDERSON *et al.* (1974). For an isotropic material, *P*-wave velocities are related to the crack density by the relation:

$$\Gamma = \left[1 - \left(\frac{P}{P_0}\right)^2\right] \Big/ (a_1 + 2a_2). \tag{8}$$

P_0 is the *P*-wave velocity of the crack-free rock and the coefficients $a_1 = 1.452$ and $a_2 = 0.192$ are taken from SOGA *et al.* (1978).

Maximum velocities P_0 and S_0 of the crack-free and fully dense materials are not known. We assume P_0 and S_0 exceed by 5% the maximum vertical components of velocities registered in our experiments (P_V and S_{HV}). For basalt $P_{0b} = 5.9$ km/s; $S_{0b} = 3.29$ km/s and for granite $P_{0g} = 6.34$ km/s; $S_{0g} = 3.88$ km/s. Equations (1)–(2) give $v_{0b} = 0.27$ and $K_{0b} = 58.3$ GPa for basalt and $v_{0g} = 0.2$ and $K_{0g} = 52.7$ GPa for granite.

Crack densities are predicted to decrease with increasing confining pressure. In all models, the estimated crack density of basalt is significantly higher than that of granite. At confining pressures > 20 MPa, there is very good agreement between the model predictions for granite (Fig. 11). For basalt at elevated pressures, the agreement is fair, but at pressures < 80 MPa and crack densities > 0.3 the Walsh model deviates more strongly from other models and predicts considerably higher crack densities than self-consistent and SOGA *et al.* (1978) models. At low pressures, the crack porosity of basalt is $> 6\times$ higher than of granite (Fig. 10), rendering the model assumption of a dilute concentration of non-interacting cracks invalid. The self-consistent approach of O'CONNELL and BUDIANSKY (1974) may account for limited interaction between individual cracks, resulting in predictions that are possibly more accurate towards low confining pressures and elevated crack densities. The approach of SOGA *et al.* (1978) predicts crack densities very similar to the self-consistent model.

4.2. The Effect of Cyclic Stress on Elastic Properties of Basalt and Granite

A wealth of studies exists investigating the effect of differential stress on the elastic properties of dry rock (e.g., PATERSON and WONG, 2005; SCHUBNEL *et al.*, this issue). In general, stress-induced anisotropy of the crack orientation distribution and the *P*-wave anisotropy and acoustic birefringence of *S*-waves are observed to increase with increasing differential stress extending to rock failure (BONNER, 1974; HADLEY, 1975; WINKLER and MURPHY, 1995). This study illustrates that *P*-wave anisotropy A_P and *S*-wave birefringence B_S increase with increasing axial strain and decreasing confining pressure. Close to failure A_P and B_S attain values of 40% and 12%,

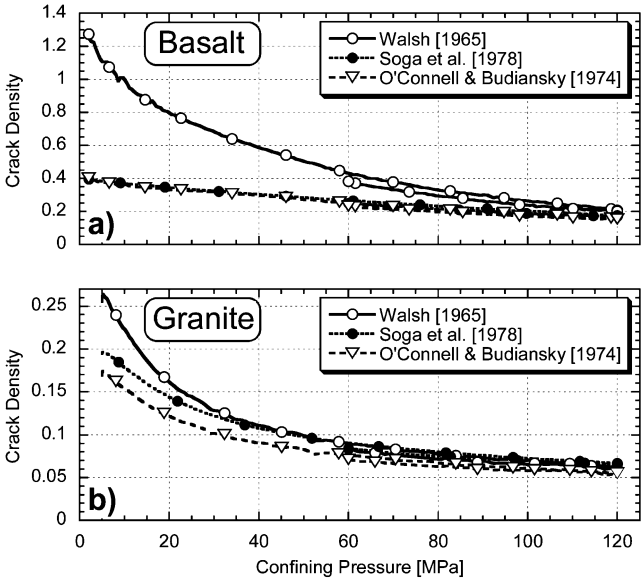

Figure 11
Crack densities of basalt sample Eb5 (a) and granite sample Ag75 (b) inverted from elastic wave velocities and from crack closure data vs. confining pressure. Open circles — predictions of WALSH (1965a); solid circles — model of SOGA *et al.* (1978), open triangles —self-consistent approximation of O'CONNELL and BUDIANSKY (1974). Model predictions for crack density in granite are in good agreement at pressures > 20 MPa; for basalt model predictions deviate significantly at pressures < 80 MPa and crack densities > 0.3.

respectively for basalt, and 35% and 20%, respectively for granite. However, a striking observation of this study is that changes in *P*-wave anisotropy and *S*-wave birefringence with increasing strain, differ significantly for basalt and granite (Figs. 6–8). For basalt, A_P and B_S increase much more rapidly at low stresses and axial strains than for granite that shows a different behavior, i.e., a significant increase of A_P and B_S at elevated stresses. At 20 MPa confining pressure and close to failure, *P*-wave anisotropy in basalt shows a rapid increase.

We attribute this behavior to the different crack microstructures of the starting basalt and granite samples. In particular, basalt contains multiple mm-scale thin cracks often associated with pyroxene inclusions. Closing of these cracks with increasing pressure at hydrostatic conditions (Fig. 5) and with increasing mean and axial stress (Figs. 6–8) produces significantly larger compaction of basalt compared to granite. Development of a strong initial *P*-wave anisotropy in basalt is related to a significant increase of the axial velocity P_V compared to P_H during initial loading (Fig. 12a). This anisotropy may be due to differential crack closure parallel and normal to the compression direction. However, for granite increasing anisotropy is

rather related to a decrease of the horizontal velocity P_H (Fig. 12c). This is due to an increasing density of dilatant cracks, with planes oriented parallel to the compression direction.

The development of an anisotropic crack orientation distribution with increasing stress and axial strain is also shown by the evolution of the crack density parameter. We applied the model of SOGA *et al.* (1978) to invert Γ from the velocity data using the equations:

$$\Gamma_H = \left[(a_1 - a_2) + a_2\left(\frac{P_V}{P_0}\right)^2 - a_1\left(\frac{P_H}{P_0}\right)^2\right] \Big/ \left(a_1^2 + a_1 a_2 - 2a_2^2\right), \tag{9a}$$

$$\Gamma_V = \left[a_1 - a_2 - (a_1 + a_2)\left(\frac{P_V}{P_0}\right)^2 + 2a_2\left(\frac{P_H}{P_0}\right)^2\right] \Big/ \left(a_1^2 + a_1 a_2 - 2a_2^2\right). \tag{9b}$$

The crack density parameters Γ_H and Γ_V refer to the densities of cracks, with planes oriented respectively parallel and perpendicular to the compression direction z, a_1 and a_2 are as in equation (8).

For basalt, crack densities Γ_H and Γ_V decrease with increasing axial strain except close to failure at 20 MPa confining pressure (Fig. 12b). The density of cracks, with crack planes oriented parallel to the compression direction (Γ_H), starts to increase rapidly at axial strains $> 0.8\%$. In granite, closure of cracks oriented perpendicular to the compression axis is far less than in basalt (Fig. 12d). The SOGA *et al.* (1978) model predicts increasing density of cracks oriented parallel to the compression axis (Γ_H) with increasing stress at 60–20 MPa confining pressure.

The model results are in good qualitative agreement with the observed acoustic emission activity and the distribution of AE source types during stress cycling. At 60 and 40 MPa pressure, AE activity in basalt is substantially less than in granite (Figs. 6d, 6h–8d,8h), suggesting that compaction of basalt largely involves closure of pre-existing cracks. At 40 MPa a significant increase of A_P and Γ_H is observed in granite at an axial strain of about 0.6%, coinciding with a strong increase in AE-activity (compare Figs. 7g, 7h, 12d). A similar observation holds for basalt and granite close to failure. Distribution of AE source types during stress cycling is different compared to the AE distribution during hydrostatic loading. Tensile AE source types dominate in both materials during stress cycling. At elevated confining pressure only basalt samples display *C*-type sources that may be related to collapsing pore space. Close to failure we found a substantial increase of shear-type events largely at the expense of tensile events.

The strong effect of stress cycling on *P*-wave anisotropy and *S*-wave birefringence at low deviatoric stresses may be even more pronounced in the field compared to our laboratory measurements, because effective elastic moduli scale with crack length and aspect ratio (WALSH, 1965a). For example, it is conceivable that loading of the Etna volcanic edifice by increasing magma pressure may result in pronounced

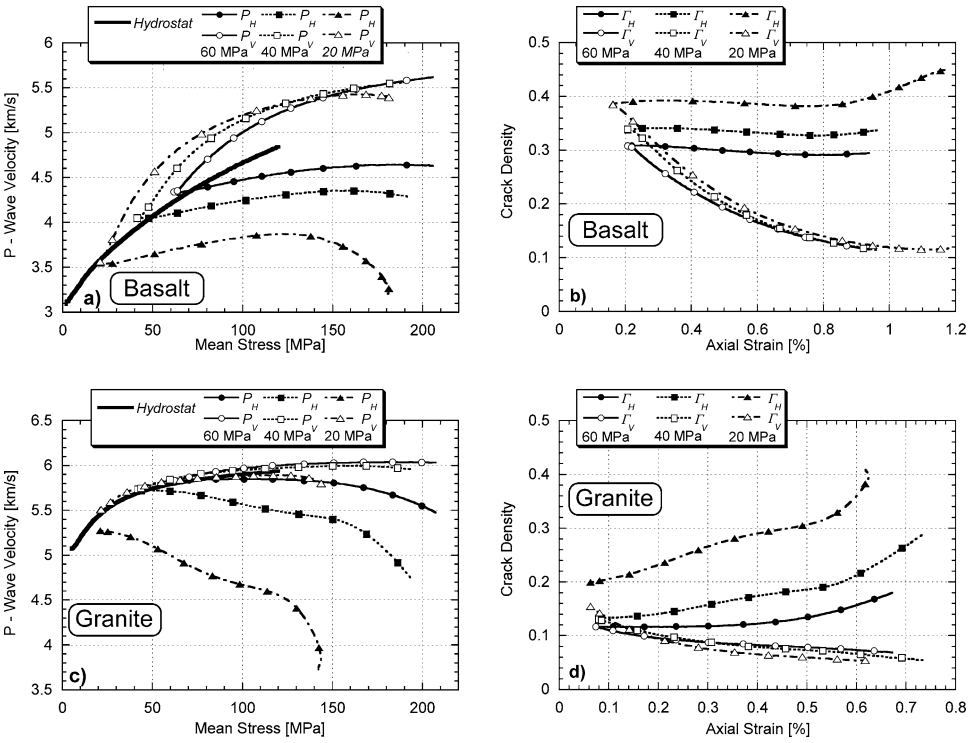

Figure 12

P wave velocity measured in horizontal (P_H) and vertical (P_V) direction during triaxial compression of basalt Eb5 (a) and granite Ag75(c). Solid symbols — horizontal components, open symbols — vertical components of *P* wave velocity, bold curve — *P* wave velocity measured during hydrostatic loading. Mean stress was calculated as $(\sigma_1 + 2\sigma_3)/3$, where σ_1 is axial stress and σ_3 is confining pressure. Crack density Γ was inverted using the model of SOGA *et al.* (1978) for Basalt Eb5 (b) and Granite Ag75 (d). Γ_H (solid symbols) is density of cracks, with planes oriented parallel to the vertical sample axis compression direction, Γ_V (open symbols) is the density of cracks, with planes oriented normal to the sample axis. Crack densities shown in (b) and (d) were estimated by inversion of *P*- wave velocity measurements presented in (a) and (c).

P-wave anisotropy and shear-wave splitting. Our results suggest that during loading anisotropy of elastic wave speeds may evolve before appreciable seismic activity occurs.

5. Conclusions

We investigated the evolution of acoustic emissions activity, compressional and shear-wave velocities, and volumetric strain of Etna basalt and Aue granite in

hydrostatic and triaxial compression tests. With increasing hydrostatic pressure to 120 MPa, *P*-wave velocities in basalt increase by > 50% and by < 20% in granite. In both materials compaction is associated with significant AE activity suggesting irreversible closure of pore space. Analysis of source types reveals dominantly *C*-type events indicating pore collapse. Compliant pore space present in basalt is at least six times larger than in granite. Static moduli estimated during hydrostatic compression are substantially lower than dynamic values. Static and dynamic moduli evince a pronounced hysteresis during a pressure cycle. Crack densities inverted from seismic velocities compare favourably with predictions from mechanical closure models at pressures > 80 MPa, but deviate significantly at lower pressures.

In triaxial compression experiments performed in pressure cycles at 20, 40, 60 MPa, pronounced *P*-wave anisotropies and shear-wave birefringence develop in both materials, but are significantly stronger in basalt than in granite. Change in ultrasonic wave speeds and evolution of anisotropy in basalt is more pronounced than in granite, particularly at low confining pressures. With increasing differential stress, AE activity in granite and basalt increased with a significant contribution of tensile events. Close to failure the relative contribution of tensile events and the speed of horizontally oriented elastic waves decreased. A concomitant increase of double-couple events indicating shear, suggests shear cracks connect previously formed tensile cracks.

Acknowledgements

We acknowledge the constructive reviews of Alexandre Schubnel and Phil Benson. Their suggestions and comments, helped to enhance the manuscript.

References

Anderson, D.L., Minster, B. and Cole, D. (1974), *The effect of oriented cracks on seismic velocities*, J. Geophys. Res. *79*, 4011–4015.

Ayling, M.R., Meredith, P.G., and Murrell, A.F. (1995), *Microcracking during triaxial deformation of porous rocks monitored by changes in rock physical properties, I. Elastic-wave propagation measurements on dry rocks*, Tectonophys. *245*, 205–221.

Benson, P., Schubnel, A., Vinciguerra, S., Trovato, C., Hazzard, J., Meredith, P.G., and Young, R.P. (2006), *Modelling the permeability evolution of micro-cracked rocks from elastic wave velocity inversion at elevated hydrostatic pressure*, J. Geophys. Res. *111*, BO4202, doi: 10.1029/2005JB03710.

Bonaccorso, A., Campisi, O., Falzone, G., Puglisi, G., Velardita, R., and Villari, L. (1990), *Ground deformation: Geodimeter trilateration and borehole tiltmetry*. In (Barberi, F., Bertagnini, A., and Landi, P., eds.), Mt. Etna 1989 Eruption, Consiglio Nazionale delle Ricerche-Gruppo Nazionale per la Vulcanologia (Giardini, Pisa, Italy 1990) pp. 44–47.

Bonner, B. P. (1974), *Shear-wave birefringence in dilating granite*, Geophys. Res. Lett. *1*, 217–220.

BRIOLE, P., NUNNARI, G., PUGLISI, G., and MURRAY, J.B. (1990), *The 1989 September-October eruption of Mt. Etna (Italy): some quantitative information obtained by geodesy and tiltmetry.*, C.R. Acad. Sci. Paris *310*, II, 1747–1754.

CASTELLANO, M., FERRUCCI, F., GODANO C., IMPOSA S. and MILANO G. (1993), *Upwards migration of seismic focii: A forerunner of the 1989 eruption of Mt Etna (Italy),* Bull. Volcanol., *55*, 357–361.

CHENG, C.H. and JOHNSTON, D. (1981), *Dynamic and static moduli*, Geophys. Res. Lett. *8*, 39–42.

DRESEN, G. and GUEGUEN, Y. (2004), *Damage and rock physical properties*. In *Mechanics of fluid-saturated Rocks* (eds. Y. GUEGUEN and M. Bouteca) pp. 169–217 (Elsevier Academic Press, Amsterdam 2004).

FERRUCCI, F., RASA, R., GAUDIOSI, G., AZZARO, R., and IMPOSA, S. (1993), *Mt. Etna: A model for the 1989 eruption*, J. Volc. Geoth. Res. *56*, 35–55.

GUEGUEN, Y., and PALCIAUSKAS, V. (1994), *Introduction to the Physics of Rocks.*, (Princeton University Press, Princeton, ISBN 0-691-03452-4). 294 pp.

HADLEY, K. (1975), *Dilatancy: Further Studies in Crystalline Rocks*, Ph.D. Thesis, 202 pp. Massachusetts Institute of Technology, Cambridge.

HADLEY, K. (1976), *Comparison of calculated and observed crack densities and seismic velocities in Westerly granite*, J. Geophys. Res. *81*, 3484–3493.

HOLCOMB, D. (1993), *General theory of the Kaiser effect*, J. Rock Mech. Min. Sci. and Geomech. Abstr. *30*, 929–935.

JANSSEN, C., WAGNER, C.F., ZANG, A., and DRESEN, G. (2001), *Fracture Process Zone in Granite: A Microstructural Analysis*, Int. J. Earth Sci. *90*, 46–59.

KING, M. S. (1969), *Static and dynamic elastic moduli of rocks under pressure*, Paper presented at Rock Mechanics-Theory and Practice, University of California, June 16–19.

LEONARD, M. and KENNETT, B.L.N. (1999), *Multi-component autoregressive techniques for the analysis of seismograms,* Phys. Earth Planet. Int. *113*(1–4), 247.

LOCKNER, D.A., WALSH, J.B., and BYERLEE, J.D. (1977), *Changes in seismic velocity and attenuation during deformation of granite*, J.Geophys. Res. *82*, 5374–5378.

MAVKO, G., MUKERJI, T., and DVORKIN, J. (1998), *The Rock Physics Handbook-Tools for Seismic Analysis in Porous Media*, 329 pp. (Cambridge University Press, Cambridge 1998).

NELDER, J. and MEAD, R. (1965). *A Simplex method for function minimization*, Computer J. *7*, 308–312.

NUR, A. (1971), *Effects of stress on velocity anisotropy in rocks with cracks*, J. Geophys. Res. *76*, 2021–2034.

O'CONNELL, R.J. and BUDIANSKY, B. (1974), *Seismic velocities in dry and saturated cracked solids*, J. Geophys. Res. *79*, 5412–5426.

PATERSON, M.S. and WONG, T.F. (2005), *Experimental Rock Deformation–The Brittle Field*, 347 pp. (Springer, Berlin).

RECHES, Z. and LOCKNER, D. A. (1994), *Nucleation and growth of faults in brittle rocks*, J. Geophys. Res. *99*, 18,159–18,173.

SCHUBNEL, A., NISHIZAWA, O., MASUDA, K., LEI, X., XUE, Z., and GUEGUEN, Y. (2003), *Velocity Measurements and crack density determination during wet triaxial experiments on Oshima and Toki granites*, Pure Appl. Geophys. *160*, 869–887.

SCHUBNEL, A., BENSON, P., THOMPSON, B.D., HAZZARD, J., and YOUNG, R.P. (2006), *Quantifying damage, saturation and anisotropy in cracked rocks by inverting elastic wave velocities*, Pure Appl. Geophys., this issue.

SIMMONS, G. and BRACE, W.F. (1965), *Comparison of static and dynamic measurements of compressibility of rocks*, J. Geophys. Res. *70*, 5649–5656.

SOGA, N., MIZUTANI, H., SPETZLER, H., and MARTIN, R. J. III. (1978), *The effect of diltancy on velocity anisotropy in Westerly Granite*, J. Geophys. Res. *83*, 4451–4458.

TAPPONNIER, P. and BRACE, W.F. (1976), *Development of stress-induced microcracks in Westerly Granite*, Int. J. Rock Mech. Min. Sci. and Geomech. *13*, 103–112.

VINCIGUERRA, S., TROVATO, C., MEREDITH, P.G. and BENSON, P.M. (2005), *Relating seismic velocities, thermal cracking and permeability in Mt. Etna and Iceland basalts*, Int. J. Rock Mech. Min. Sci. *42*/7-8, 900–910.

WALSH, J.B. (1965a), *The effect of cracks on the compressibility of rock*, J. Geophys. Res. *70*, 381–389.

WALSH, J.B. (1965b), *The effect of cracks on the uniaxial elastic compression of rocks*, J. Geophys. Res. *70*, 399–411.

WINKLER, K. W. and MURPHY III, W. F. *Acoustic velocity and attenuation in porous rocks*, In *Rock Physics and Phase Relations*, AGU Reference Shelf (ed. T. J. Ahrens) pp. 20–34 (AGU, Washington (1995)

ZANG, A., WAGNER, F.C., STANCHITS, S., DRESEN, G., ANDRESEN, R. and HAIDEKKER, M.A. (1998), Source analysis of acoustic emissions in Aue granite cores under symmetric and asymmetric compressive loads, Geophys. J. Int. *135*, 1113–1130.

ZANG, A., WAGNER, F.C., STANCHITS, S., JANSSEN, C., and DRESEN, G. (2000), *Fracture process zone in granite*, J. Geophys. Res. *105*, 23651–23661.

(Received May 20, 2005, revised November 3, 2005, accepted November 4, 2005)